2DNMR data inversion using locally adapted multi-penalty regularization

Noname manuscript No.
(will be inserted by the editor)

2DNMR data inversion using locally adapted multi-penalty regularization

Villiam Bortolotti · Germana Landi · Fabiana Zama

Received: date / Accepted: date

Abstract Geologists and Reservoir Engineers routinely use time-domain nuclear magnetic resonance (NMR) to learn about the porous structure of rocks that hold underground fluids. In particular, two-dimensional NMR (2DNMR) technique is now gaining importance in a wide variety of applications. Crucial issues in 2DNMR analysis are the speed, robustness and accuracy of the data inversion process. This paper proposes a multi-penalty method with locally adapted regularization parameters for fast and accurate inversion of 2DNMR data.

The method solves an unconstrained optimization problem whose objective function contains a data-fitting term, a single $L1$ penalty parameter and a multiple parameter $L2$ penalty. We propose an adaptation of the Fast Iterative Shrinkage and Thresholding (FISTA) method to solve the multi-penalty minimization problem, and an automatic procedure to compute all the penalty parameters. This procedure generalizes the Uniform Penalty principle introduced in [Bortolotti et al., *Inverse Problems*, 33(1), 2016].

The proposed approach allows us to obtain accurate 2D relaxation time distributions while keeping short the computation time. Results of numerical experiments on synthetic and real data prove that the proposed method is efficient and effective in reconstructing the peaks and the flat regions that usually characterize 2DNMR relaxation time distributions.

Keywords NMR relaxometry · multi-parameter regularization · multi-penalty regularization · UPEN2D · FISTA

1 Introduction

Geologists and Reservoir Engineers routinely use time-domain nuclear magnetic resonance (NMR) to learn about the porous structure of rocks that hold underground fluids. NMR is a unique technique that directly senses the presence of ^{1}H nuclei. Therefore, it permits to accurately estimate many petrophysical parameters, such as porosity, saturation and permeability, etc. Thus nowadays, for example, borehole ^{1}H NMR is extensively used in oil and gas reservoir characterisation, and recent technological advances have led to tools suitable for environmental applications (see details in [1]). Moreover, two-dimensional NMR (2DNMR) techniques are

Villiam Bortolotti
Department of Civil, Chemical, Environmental, and Materials Engineering, University of Bologna
E-mail: villiam.bortolotti@unibo.it

Germana Landi
Department of Mathematics, University of Bologna
E-mail: germana.landi@unibo.it

Fabiana Zama
Department of Mathematics, University of Bologna
E-mail: fabiana.zama@unibo.it

gaining increasing importance in analysing different porous media ranging from cement to biological tissues. Therefore, an appropriate inversion algorithm of NMR relaxation data is a crucial requirement [4].

In 2DNMR, for example, the joint measurements of the spin relaxation with respect to the longitudinal and transverse relaxation parameters T_1 and T_2, respectively, allow us to build two-dimensional relaxation time distributions ($T_1 - T_2$ maps). Peaks usually characterize such distributions over flat regions; the position and volume of the peaks are used to obtain information such as petrophysical properties, molecular diffusion, etc [4]. Due to the large dimension of the data and the inherent ill-posedness of the inverse problem, a significant issue in 2DNMR inversion is to ensure both computational efficiency and accuracy. This aspect is particularly relevant in multidimensional logging where 3DNMR inversion algorithms are usually based on methods for 2DNMR inversion [2]. Therefore, the development and application of 3DNMR techniques is seriously restricted by the efficiency and accuracy of the 2D inversion [5]. The measured NMR data S are related to the NMR parameter distribution F according to a Fredholm integral equation of the first kind with separable kernel. For example, in case of $T_1 - T_2$ 2D distributions (2DNMR maps) we have the following continuous model:

$$S(t_1, t_2) = \int_0^\infty\!\!\int k_1(t_1, T_1) k_2(t_2, T_2) F(T_1, T_2)\ dT_1\ dT_2 + e(t_1, t_2) \tag{1}$$

where t_1, t_2 are the evolution time parameters and $e(t_1, t_2)$ represents additive Gaussian noise. The kernels $k_1(t_1, T_1)$ and $k_2(t_2, T_2)$ are decaying exponential functions.The discretization of the integral equation (1) by a quadrature rule leads to a linear inverse problem

$$\mathbf{K}\mathbf{f} + \mathbf{e} = \mathbf{s} \tag{2}$$

where $\mathbf{K} = \mathbf{K}_2 \otimes \mathbf{K}_1$ is the Kronecker product of the discretized decaying exponential kernels $\mathbf{K}_1 \in \mathbb{R}^{M_1 \times N_1}$ and $\mathbf{K}_2 \in \mathbb{R}^{M_2 \times N_2}$. The vector $\mathbf{s} \in \mathbb{R}^M$, $M = M_1 \cdot M_2$, represents the measured noisy signal, $\mathbf{f} \in \mathbb{R}^N$, $N = N_1 \cdot N_2$, is the vector reordering of the 2D distribution to be computed and $\mathbf{e} \in \mathbb{R}^M$ represents the additive Gaussian noise. The severe ill-conditioning of $\mathbf{K}$ is well-known, and it causes the least-squares solution of (2) to be extremely sensitive to the noise; for this reason, regularization is usually applied. The most common numerical strategies are based on $L2$ regularization and often use constraints, such as non-negativity constraints, in order to prevent unwanted unphysical results in the computed distribution. This approach requires solving the nonnegatively constrained Tikhonov-like problem:

$$\min_{\mathbf{f} \geq 0} \left\{ \|\mathbf{K}\mathbf{f} - \mathbf{s}\|^2 + \lambda \|\mathbf{f}\|^2 \right\} \tag{3}$$

where $\lambda > 0$ is the regularization parameter. Here and henceforth $\|\cdot\|$ denotes the Euclidean norm. In this context, the approach of Venkataramanan et al. [6], uses data compression to reduce the size of problem (3) and the Butler–Reeds–Dawson method [7] to solve the smaller-size optimization problem. Chouzenoux et al. [8] apply the interior point method for the solution of (3). The main drawback of single parameter $L2$ regularization is its tendency to either over-smooth the solution, making it difficult to detect low-intensity peaks, or to under-smooth the solution creating non-physical sharp peaks. Substantial improvements are obtained by the application of multiple parameters Tikhonov regularization, as in the UPEN2D algorithm [10,11] which solves the minimization problem

$$\min_{\mathbf{f} \geq 0} \left\{ \|\mathbf{K}\mathbf{f} - \mathbf{s}\|^2 + \sum_{i=1}^{N} \lambda_i (\mathbf{L}\mathbf{f})_i^2 \right\} \tag{4}$$

where $\mathbf{L} \in \mathbb{R}^N$ is the discrete Laplacian operator. The multiple regularization parameters λ_is are locally adapted, i.e., at each iteration, approximated values for the λ_is are computed by imposing the Uniform Penalty (UPEN) principle [10] and a constrained subproblem is solved by the Newton Projection method [12]. Although UPEN2D can obtain very accurate distributions, as reported in the literature [10,13,14,11], its computational cost may be high since it requires the solution of several nonnegatively constrained least-squares problems. In the NMR literature, $L1$ regularization has been recently considered in order to better reproduce the characteristic sparsity of the relaxation distribution. In [15], the $L1$ regularization problem

$$\min_{\mathbf{f}} \left\{ \|\mathbf{K}\mathbf{f} - \mathbf{s}\|^2 + \alpha \|\mathbf{f}\|_1 \right\} \tag{5}$$

is considered and the Fast Iterative Shrinkage-Thresholding Algorithm (FISTA) [16] is used for its solution. An update searching method is proposed to iteratively determine the regularization parameter as $\alpha = \sqrt{N}\sigma/\|\mathbf{f}\|_1$ where σ is the standard deviation of the noise. We remark that FISTA is known to be one of the most effective and efficient methods for solving $L1$-based image denoising and deblurring problems. Recently, FISTA has also been applied to non-convex regularization [17,18].

The $L1$ regularization has also been used in NMR to decrease the data acquisition time [19]. In [20], an algorithm related to FISTA is applied to NMR relaxation estimation and comparisons with the methods of Venkataramanan et al. [6], and Chouzenoux et al. [8], are carried out showing the efficiency of the FISTA-like method. However, despite its computational efficiency and its capability of revealing isolated narrow peaks, $L1$ regularization tends to divide a wide peak or tail into separate undesired peaks.

Recently, the elastic net method [21] with a non-negative constraint

$$\min_{\mathbf{f}\geq 0}\left\{\|\mathbf{Kf}-\mathbf{s}\|^2+\lambda\|\mathbf{f}\|^2+\alpha\|\mathbf{f}\|_1\right\} \tag{6}$$

has been used in [22] to obtain $T2$ distributions. The problem is formulated as a linearly constrained convex optimization problem and the primal-dual interior method for convex objectives has been applied to one dimensional [22] and two dimensional [23] NMR relaxation problems. However, the performance of the method depends on the two regularization parameters which needs an accurate tuning; a parameter selection analysis is performed in [23] for a specific set of 2DNMR data.

Our previous review of the current literature shows that for each inversion method, we have to take into account both the efficiency and the accuracy. The UPEN2D method has a great inversion accuracy due to the employment of multi-penalty regularization with locally adapted parameters, but the nonnegative constraints are responsible for its poor computational efficiency. The $L1$ regularization with FISTA algorithm is computationally very efficient, but its accuracy can be low in the presence of non-isolated peaks. Multi-penalty regularization (6) is able to simultaneously promote distinct features of the sought-for distribution, since it yields a good trade-off among data fitting error, sparsity and smoothness of the solution. However, its applicability is greatly limited by the fact that multiple parameters tuning is a challenging task depending on SNR, sparsity and smoothness. To overcome the aforementioned drawbacks ensuring both efficiency and accuracy, in this paper, we propose a multi-penalty approach involving $L1$ and $L2$ penalties with locally adapted regularization parameters. The proposed method can be mathematically formulated as the unconstrained minimization problem

$$\min_{\mathbf{f}}\left\{\|\mathbf{Kf}-\mathbf{s}\|^2+\sum_{i=1}^{N}\lambda_i(\mathbf{Lf})_i^2+\alpha\|\mathbf{f}\|_1\right\}. \tag{7}$$

This approach allows us to accurately reconstruct distributions with isolated and non-isolated peaks as well as flat areas, in short computation time. On the one hand, $L1$ regularization prevents from over-smoothing while, on the other hand, local $L2$ regularization prevents from under-smoothing merging peaks or peak tails. Since $L1$ regularization enforces sparse distributions, the nonnegative constraints are not included in problem (7) and FISTA can be used for its efficient and effective solution. The UPEN principle is extended to the multi-penalty problem (7) obtaining a very efficient computation strategy for all the regularization parameters. Therefore, tedious multiple parameters tuning procedure is not necessary.

The contribution of this paper is two-fold. Firstly, it introduces a locally adapted multi-penalty model for 2D NMR data inversion, and it proposes an efficient strategy for the automatic computation of the multiple parameters. Secondly, we prove that the solution of (7) is a regularized solution of problem (2). The extension of the regularization properties of the UPEN principle [Bortolotti et al., *Inverse Problems*, 33(1), 2016] to a multiple regularization context makes it possible to apply it to more general, non-differentiable and possibly non-convex penalties.

The proposed algorithm has been tested on both synthetic and real NMR relaxometry problems, and has been compared to multiple parameters $L2$ regularization (4) (UPEN2D) and to $L1$ regularization (5). The numerical results show the efficiency and effectiveness of the method.

The remainder of the paper is organized as follows: section 2 analyzes the regularization properties of the proposed method. Section 3 reports the details of the numerical algorithm. Finally, in section 4, some results are shown and discussed both on synthetic and real NMR data. The algorithms are implemented in Matlab R2019b and are freely distributed upon request to the authors.

2 The Uniform Penalty Principle

In order to generalize to multi-penalty regularization the UPEN principle introduced in [10] for problem (4), let us write problem (7) as

$$\min_{\mathbf{f}} \left\{ \|\mathbf{K}\mathbf{f} - \mathbf{s}\|^2 + \sum_{i=1}^{N+1} \eta_i \phi_i(\mathbf{f}) \right\} \tag{8}$$

where

$$\phi_i(\mathbf{f}) = \begin{cases} (\mathbf{L}\mathbf{f})_i^2, \ i = 1, \ldots, N, \\ \|\mathbf{f}\|_1, \quad i = N+1, \end{cases} \quad \text{and} \quad \eta_i = \begin{cases} \lambda_i, \ i = 1, \ldots, N, \\ \alpha, \ \ i = N+1. \end{cases} \tag{9}$$

The generalization of the UPEN principle can be stated as follows.

Definition 2.1 (Generalized Uniform Penalty Principle)**.** *Choose the regularization parameters η_i of multi-penalty regularization (8) such that, at a solution $\mathbf{f}$, the terms $\eta_i \phi_i(\mathbf{f})$ are constant for all i with $\phi_i(\mathbf{f}) \neq 0$, i.e:*

$$\eta_i \phi_i(\mathbf{f}) = c, \quad \forall\, i = 1, \ldots, N+1 \quad s.t. \quad \phi_i(\mathbf{f}) \neq 0 \tag{10}$$

where c is a positive constant.

Let us assume that a suitable bound ε on the fidelity term of the exact solution $\mathbf{f}^*$ is given; i.e:

$$\|\mathbf{K}\mathbf{f}^* - \mathbf{s}\|^2 \leq \varepsilon^2 \tag{11}$$

where $\mathbf{f}^*$ is the solution of the noise-free least-squares problem

$$\min_{\mathbf{f}} \left\{ \|\mathbf{K}\mathbf{f} - \hat{\mathbf{s}}\|^2, \ \mathbf{s} = \hat{\mathbf{s}} + \mathbf{e} \right\}. \tag{12}$$

Following Miller's criterium [24], the constant c is selected to balance the fidelity and regularization terms in (8); i.e:

$$c = \frac{\varepsilon^2}{N_0} \tag{13}$$

where N_0 is the number of non null terms $\phi_i(\mathbf{f})$:

$$N_0 = \#\{i \mid \phi_i(\mathbf{f}) \neq 0, \ i = 1, \ldots, N+1\}. \tag{14}$$

Obviously, with this choice for c, Lemma 3.1 of [10] still applies. The lemma is restated here for the sake of clarity.

Lemma 2.1. *If $\mathbf{f}$ satisfies $\|\mathbf{K}\mathbf{f} - \mathbf{s}\|^2 \leq \varepsilon^2$ and the parameters η_i, $i = 1, \ldots, N+1$, are chosen according to the generalized uniform penalty principle with*

$$0 \leq c = \frac{\varepsilon^2}{N_0} \tag{15}$$

where N_0 is the number of non null terms $\phi_i(\mathbf{f})$, then

$$0 \leq \|\mathbf{K}\mathbf{f} - \mathbf{s}\|^2 + \sum_{i=1}^{N_0} \eta_i \phi_i(\mathbf{f}) \leq 2\varepsilon^2. \tag{16}$$

Conversely, if $\mathbf{f}$ satisfies (16) and the generalized UPEN principle with (15), then it also satisfies $\|\mathbf{K}\mathbf{f} - \mathbf{s}\|^2 \leq \varepsilon^2$.

Proof. Let $\mathbf{f}$ be such that $\|\mathbf{Kf}-\mathbf{s}\|^2 \leq \varepsilon^2$, then, if (10) holds with c selected as in (15), we have

$$0 \leq \|\mathbf{Kf}-\mathbf{s}\|^2 + \sum_{i=1}^{N_0} \eta_i \phi_i(\mathbf{f}) \leq \varepsilon^2 + \sum_{i=1}^{N_0} \frac{\varepsilon^2}{N_0} = 2\varepsilon^2. \tag{17}$$

Conversely, if (16) and (15) hold, then

$$2\varepsilon^2 \geq \|\mathbf{Kf}-\mathbf{s}\|^2 + \sum_{i=1}^{N_0} \eta_i \phi_i(\mathbf{f}) = \|\mathbf{Kf}-\mathbf{s}\|^2 + \sum_{i=1}^{N_0} \frac{\varepsilon^2}{N_0} = \|\mathbf{Kf}-\mathbf{s}\|^2 + \varepsilon^2. \tag{18}$$

Hence

$$\|\mathbf{Kf}-\mathbf{s}\|^2 + \varepsilon^2 \leq 2\varepsilon^2$$

and, by subtraction, we obtain the thesis:

$$\|\mathbf{Kf}-\mathbf{s}\|^2 \leq \varepsilon^2$$

□

From (10) and (13) we obtain the following expression for the η_i's:

$$\eta_i = \frac{\varepsilon^2}{N_0 \phi_i(\mathbf{f})} \quad \text{for all} \quad i = 1, \ldots, N+1 \quad \text{such that} \quad \phi_i(\mathbf{f}) \neq 0 \tag{19}$$

which can be written in terms of the parameters λ_i and α as

$$\lambda_i = \frac{\varepsilon^2}{N_0 (\mathbf{Lf})_i^2} \quad \text{if} \quad (\mathbf{Lf})_i \neq 0 \quad \text{and} \quad \alpha = \frac{\varepsilon^2}{N_0 \|\mathbf{f}\|_1}. \tag{20}$$

If the regularization parameters are computed as in (20), the following lemma shows that the solution of (7) is a regularized solution of (2).

Lemma 2.2. *Let $\mathbf{f}^*$ be the solution of the noise-free least-squares problem (12) and let $\mathbf{f}_\varepsilon$ denote the solution to problem (7) where the regularization parameters are chosen according to the generalized uniform penalty principle as follows:*

$$\lambda_i = \begin{cases} \dfrac{\varepsilon^2}{N_0 (\mathbf{Lf}^*)_i^2}, & \text{if } (\mathbf{Lf}^*)_i \neq 0; \\ \gamma \varepsilon^2, & \text{otherwise;} \end{cases} \quad \text{and} \quad \alpha = \frac{\varepsilon^2}{\|\mathbf{f}^*\|_1} \tag{21}$$

where γ is a positive constant and N_0 is the number of non null terms $(\mathbf{Lf}^*)_i$. Then

$$\lim_{\varepsilon \to 0} \mathbf{f}_\varepsilon = \mathbf{f}^*$$

and hence $\mathbf{f}_\varepsilon$ is a regularized solution of (2).

Proof. Let us define the diagonal matrix $\mathbf{\Lambda}$ whose diagonal elements are the parameters λ_i. The first-order optimality conditions of (7) are

$$\{\mathbf{0}\} \in 2\mathbf{K}^T(\mathbf{Kf}-\mathbf{s}) + 2\mathbf{L}^T\mathbf{\Lambda}\mathbf{Lf} + \alpha\mathbf{g} \tag{22}$$

where $\mathbf{g}$ is the subgradient of $\|\mathbf{f}\|_1$, i.e. [3, chp. 3]:

$$g_i = \begin{cases} +1, & \text{if } f_i > 0 \\ -1, & \text{if } f_i < 0 \\ [-1, 1], & \text{if } f_i = 0 \end{cases}, \quad i = 1, \ldots, N.$$

In the limit for $\varepsilon \to 0$, from (20), equation (22) becomes

$$\{\mathbf{0}\} \in 2\mathbf{K}^T(\mathbf{Kf}-\mathbf{s}) \tag{23}$$

which are the first-order optimality conditions for (12). □

3 The proposed method

The computation of the parameters λ_i, $i = 1, \ldots, N$, and α as in (21) uses the quantities $\mathbf{f}^*$ and ε which are unknown. For this reason, we propose a splitting iterative procedure where they are respectively approximated by the $k-$th iterate $\mathbf{f}^{(k)}$ and the corresponding residual norm $\|\mathbf{K}\mathbf{f}^{(k)} - \mathbf{s}\|$. The proposed iterative procedure is outlined in Algorithm 1 where τ is the tolerance of the stopping criterium. The parameter ρ is a compliance floor that prevents possible divisions by zero, occurring when $(\mathbf{L}\mathbf{f}^{(k)})_i \simeq 0$. If ρ is too small the correspondent value λ_i may become too large, making the problem very badly conditioned and hence numerically unstable. On the contrary, if ρ is too large, only L1 penalty affects the solution because $\lambda_i \simeq 0$.

Algorithm 1

1: Compute a starting guess $\mathbf{f}^{(0)}$;
2: Choose $\rho, \tau \in (0, 1)$; set $k = 0$;
3: **repeat**
4: Set $\epsilon^{(k)} = \|\mathbf{K}\mathbf{f}^{(k)} - \mathbf{s}\|^2$
5: Set $\lambda_i^{(k)} = \dfrac{\epsilon^{(k)}}{(N+1)(\mathbf{L}\mathbf{f}^{(k)})_i^2 + \rho}$, $i = 1, \ldots N$
6: Set $\alpha^{(k)} = \dfrac{\epsilon^{(k)}}{(N+1)\|\mathbf{f}^{(k)}\|_1}$
7: Compute

$$\mathbf{f}^{(k+1)} = \arg\min_{\mathbf{f}} \left\{ \|\mathbf{K}\mathbf{f} - \mathbf{s}\|^2 + \sum_{i=1}^{N} \lambda_i^{(k)} (\mathbf{L}\mathbf{f})_i^2 + \alpha^{(k)} \|\mathbf{f}\|_1 \right\}$$

8: Set $k = k + 1$
9: **until** $\|\mathbf{f}^{(k+1)} - \mathbf{f}^{(k)}\| \leq \tau \|\mathbf{f}^{(k)}\|$

The computation of each new approximate solution $\mathbf{f}^{(k+1)}$ at step 7 of Algorithm 1 is obtained by FISTA [16], after suitable reformulation of the minimization problem.
Let us assume that the values $\lambda_i^{(k)}$, $i = 1, \ldots, N$, and $\alpha^{(k)}$ are fixed, then problem (7) can be written as:

$$\min_{\mathbf{f}} \{\Psi_1(\mathbf{f}) + \Psi_2(\mathbf{f})\} \tag{24}$$

where:

$$\Psi_1(\mathbf{f}) = \left\| \begin{pmatrix} I & \mathbf{0} \\ \mathbf{0} & \sqrt{\mathbf{\Lambda}^{(k)}} \end{pmatrix} \begin{pmatrix} \mathbf{K} \\ \mathbf{L} \end{pmatrix} \mathbf{f} - \begin{pmatrix} \mathbf{s} \\ 0 \end{pmatrix} \right\|^2, \quad \mathbf{\Lambda}^{(k)} = \mathrm{diag}(\lambda_i^{(k)})$$

$I \in \mathbb{R}^{M \times M}$ is the Identity matrix, $\mathbf{0} \in \mathbb{R}^{M \times N}$ is a zero block, and

$$\Psi_2(\mathbf{f}) = \alpha^{(k)} \|\mathbf{f}\|_1.$$

The FISTA steps for the solution of (24) are reported in Algorithm 2 where ξ is a constant stepsize and the starting guess corresponds to solution computed in Algorithm 1 at the k-th step. The FISTA iterations are stopped when the relative distance between two successive values of the objective function of (24) becomes smaller than a given tolerance value τ_{FISTA}. At step 4 of Algorithm 2, the components of $\mathbf{f}^{(j)}$ are computed explicitly, element-wise, by means of the soft thresholding operator:

$$\mathbf{f}_i^{(j)} = \mathrm{sign}\left(z_i^{(j)} - \frac{\alpha}{\xi}\right) \max\left(\left|z_i^{(j)}\right| - \frac{\alpha}{\xi}, 0\right), \quad i = 1, \ldots, N$$

where

$$\mathbf{z}^{(j)} = \mathbf{y}^{(j)} - \frac{1}{\xi} \nabla(\Psi_1(\mathbf{y}^{(j)})).$$

Algorithm 2 – $\mathbf{f}^{k+1} = \text{FISTA\_STEP}(\xi, \mathbf{f}^{(k)}, \Psi_1, \Psi_2))$

1: Set $t_0 = 1$; $j = 0$; $\mathbf{y}^{(1)} = \mathbf{f}^{(k)}$
2: **repeat**
3: $\quad j = j + 1$
4: $\quad \mathbf{f}^{(j)} = \arg\min_{\mathbf{f}} \left\{ \Psi_2(\mathbf{f}) + \frac{\xi}{2} \left\| \mathbf{f} - \left(\mathbf{y}^{(j)} - \frac{1}{\xi} \nabla(\Psi_1(\mathbf{y}^{(j)})) \right) \right\|_2 \right\}$
5: $\quad t_{j+1} = \frac{1}{2} \left(1 + \sqrt{1 + 4t_j^2} \right)$
6: $\quad \mathbf{y}^{(j+1)} = \mathbf{f}^{(j)} + \frac{(t_j^2 - 1)}{t_{j+1}} \left(\mathbf{f}^{(j)} - \mathbf{f}^{(j-1)} \right)$
7: **until** stopping criterion
8: $\mathbf{f}^{(k+1)} = \mathbf{f}^{(j+1)}$

The convergence of FISTA has been proven for any stepsize ξ such that $\xi \geq \mathcal{L}(\Psi_1)$, where $\mathcal{L}(\Psi_1)$ is the Lipschitz constant for the gradient $\nabla\Psi_1$ [16]; i.e:

$$\mathcal{L}(\Psi_1) = \lambda_{\max}(\mathbf{K}^T\mathbf{K} + \mathbf{L}^T\mathbf{\Lambda}^{(k)}\mathbf{L}) \tag{25}$$

where $\lambda_{\max}(\mathbf{X})$ represents the maximum eigenvalue of the matrix $\mathbf{X}$.
The following theorem shows that an upper bound for $\mathcal{L}(\Psi_1)$ can be easily provided, thus obtaining the convergence of FISTA.

Theorem 3.1. *Let $\sigma_1^{(1)}$ and $\sigma_1^{(2)}$ be the maximum singular values of the matrices $\mathbf{K}_1$ and $\mathbf{K}_2$, respectively, and let $\lambda_i^{(k)}$ be the local regularization parameters computed at kth step of Algorithm 1, then the value ξ defined as follows:*

$$\xi = \left(\sigma_1^{(1)} \sigma_1^{(2)} \right)^2 + 64 \max_i |\lambda_i^{(k)}| \tag{26}$$

satisfies

$$\xi \geq \mathcal{L}(\Psi_1)$$

and it guarantees the convergence of the FISTA method.

Proof. We recall that the spectral norm of the symmetric matrix $\mathbf{K}^T\mathbf{K} + \mathbf{L}^T\mathbf{\Lambda}^{(k)}\mathbf{L}$ is defined as

$$\|\mathbf{K}^T\mathbf{K} + \mathbf{L}^T\mathbf{\Lambda}^{(k)}\mathbf{L}\|_2 = \lambda_{\max}(\mathbf{K}^T\mathbf{K} + \mathbf{L}^T\mathbf{\Lambda}^{(k)}\mathbf{L}).$$

Then, by using the triangular inequality,

$$\|\mathbf{K}^T\mathbf{K} + \mathbf{L}^T\mathbf{\Lambda}^{(k)}\mathbf{L}\|_2 \leq \|\mathbf{K}^T\mathbf{K}\|_2 + \|\mathbf{L}^T\mathbf{\Lambda}^{(k)}\mathbf{L}\|_2$$

we obtain

$$\lambda_{\max}(\mathbf{K}^T\mathbf{K} + \mathbf{L}^T\mathbf{\Lambda}^{(k)}\mathbf{L}) \leq \lambda_{\max}(\mathbf{K}^T\mathbf{K}) + \lambda_{max}(\mathbf{L}^T\mathbf{\Lambda}^{(k)}\mathbf{L})$$

since $\mathbf{K}^T\mathbf{K}$ and $\mathbf{L}^T\mathbf{\Lambda}^{(k)}\mathbf{L}$ are symmetric matrices. Using the Kronecker product properties of the Singular Value Decomposition (SVD), we have:

$$\lambda_{\max}(\mathbf{K}^T\mathbf{K}) = \lambda_{\max}((\mathbf{K}_2 \otimes \mathbf{K}_1^T)^T(\mathbf{K}_2 \otimes \mathbf{K}_1^T)) = (\sigma_1^{(1)}\sigma_1^{(2)})^2. \tag{27}$$

Concerning the term $\lambda_{\max}(\mathbf{L}^T\mathbf{\Lambda}^{(k)}\mathbf{L})$ we can apply the property of the discrete Laplacian matrix $\lambda_{\max}(\mathbf{L}) \leq 8$. This property easily follows from a structured finite difference representation of the Laplace opeartor with unit step size. Hence:

$$\lambda_{\max}(\mathbf{L}^T\mathbf{\Lambda}\mathbf{L}) \leq 64 \max_i |\lambda_i^{(k)}|. \tag{28}$$

Finally, collecting the terms (27) and (28), we obtain the value ξ that guarantees the convergence of FISTA steps. □

We observe that, in NMR, the matrices $\mathbf{K}_1$ and $\mathbf{K}_2$ are usually of small size and their SVD can be easily performed in order to compute the values $\sigma_1^{(1)}$ and $\sigma_1^{(2)}$.

Following the observations in [10], we apply Algorithm 1 with the following $L2$ penalty parameters, which have proven to be very efficient with NMR problems:

$$\lambda_i^{(k)} = \frac{\|\mathbf{K}\mathbf{f}^{(k)} - \mathbf{s}\|^2}{(N+1)\left(\beta_0 + \beta_p \max_{\mu \in I_i}(\mathbf{p}_\mu^{(k)})^2 + \beta_c \max_{\mu \in I_i}(\mathbf{c}_\mu^{(k)})^2\right)}, \quad i = 1, \ldots, N \tag{29}$$

where

$$\mathbf{c}^{(k)} = \mathbf{L}\mathbf{f}^{(\mathbf{k})}, \quad \mathbf{p}^{(k)} = \mathrm{vec}\big(\|\nabla \mathbf{F}^{(k)}\|\big), \quad \mathbf{f}^{(k)} = \mathrm{vec}(\mathbf{F}^{(k)})$$

and $\mathbf{F}^{(k)}$ is the k-th distribution map (here, vec($\mathbf{V}$) denotes the vector obtained by columnwise reordering the elements of a matrix $\mathbf{V}$). The I_i are the indices subsets related to the neighborhood of the point i and the β's are positive parameters; β_0 prevents division by zero and is a compliance floor, which should be small enough to prevent under-smoothing, and large enough to avoid over-smoothing. The optimum value of β_0, β_c and β_p can change with the nature of the measured sample.

Finally, the proposed procedure is stated in Algorithm 3 and is called L1LL2 method, which comes from "method based on $L1$ and Locally adapted $L2$ penalties". As already discussed in [10], the starting guess $\mathbf{f}^{(0)}$ is computed by applying a few iterations of the Gradient Projection method to the nonnegatively constrained least squares problem

$$\min_{\mathbf{f} \geq 0} \|\mathbf{K}\mathbf{f} - \mathbf{s}\|^2.$$

Algorithm 3 – L1LL2 method

1: Choose $\tau \in (0,1)$ and $\beta_0, \beta_p, \beta_c > 0$
2: Set $k = 0$ and compute $\mathbf{f}^{(0)}$
3: Compute $\sigma_1^{(1)}$ and $\sigma_1^{(2)}$
4: **repeat**
5: Set $\epsilon^{(k)} = \|\mathbf{K}\mathbf{f}^{(k)} - \mathbf{s}\|^2$
6: Set $\lambda_i^{(k)} = \dfrac{\epsilon^{(k)}}{(N+1)\left(\beta_0 + \beta_p \max_{\mu \in I_i}(\mathbf{p}_\mu^{(k)})^2 + \beta_c \max_{\mu \in I_i}(\mathbf{c}_\mu^{(k)})^2\right)}$, $i = 1, \ldots, N$
7: Set $\alpha^{(k)} = \dfrac{\epsilon^{(k)}}{(N+1)\|\mathbf{f}^{(k)}\|_1}$
8: Set $\xi^{(k)} = \left(\sigma_1^{(1)}\sigma_1^{(2)}\right)^2 + 64 \max_i |\lambda_i^{(k)}|$
9: Compute

$$\mathbf{f}^{(k+1)} = \textsc{fista\_step}(\xi^{(k)}, \mathbf{f}^{(k)}, \|\mathbf{K}\mathbf{f} - \mathbf{s}\|^2 + \sum_{i=1}^{N} \lambda_i^{(k)} (\mathbf{L}\mathbf{f})_i^2, \alpha^{(k)}\|\mathbf{f}\|_1)$$

10: **until** $\|\mathbf{f}^{(k+1)} - \mathbf{f}^{(k)}\| \leq \tau \|\mathbf{f}^{(k)}\|$

4 Numerical Results

The analysis of the proposed algorithm is carried out in this section both on synthetic and real NMR relaxation data. The numerical tests are performed on a PC laptop equipped with 2,9 GHz Intel Core i7 quad-core, 16 GB RAM. The algorithms are implemented in Matlab R2019b. The values $\tau = 10^{-3}$ and $\tau_{\text{FISTA}} = 10^{-7}$ have been fixed for the stopping tolerances of L1LL2 (Algorithm 3) and FISTA (Algorithm 2) respectively.

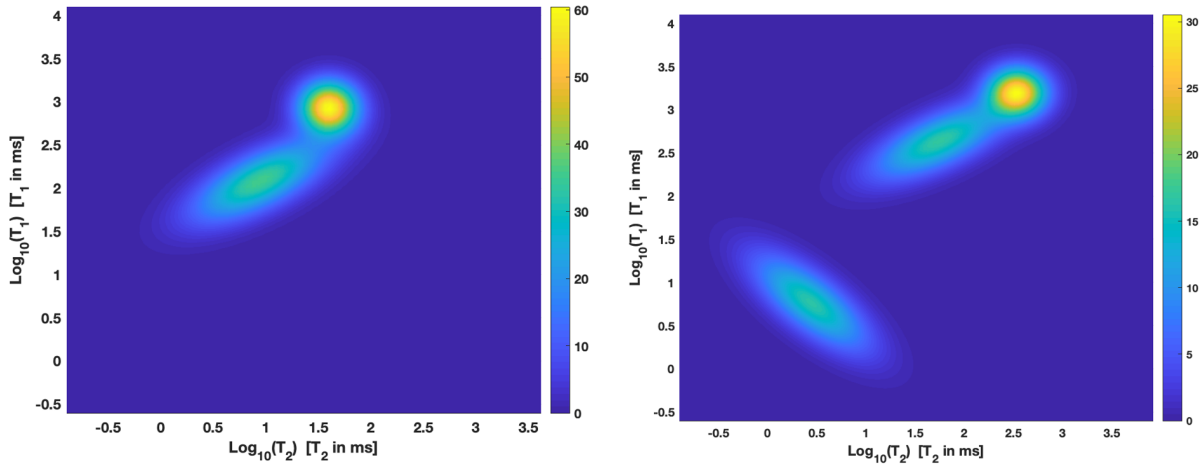

(a) Two peaks map (b) Three peaks map

Fig. 1 Maps of relaxation times used in tests with synthetic data.

4.1 Synthetic data

Aim of this paragraph is to analyse the accuracy and performance of the proposed L1LL2 algorithm. To this purpose we test L1LL2 algorithm on synthetic data that emulates the results of measurement with a 2D IR-CPMG sequence (see [10,13,14]), where the kernels of (1) are defined as follows:

$$k_1(t_1, T_1) = 1 - 2\exp(-t_1/T_1), \quad k_2(t_2, T_2) = \exp(-t_2/T_2). \tag{30}$$

Two different predefined relaxation maps $F(T_1, T_2)$ are used to compute two set of synthetic relaxation data. The first relaxation map, named `2Pks` test, has size $N_1 \times N_2$ where $N_1 = N_2 = 80$. The relaxation map, represented in Figure 1(a), has two peaks at positions ($T_1 = 814.97\ ms, T_2 = 4.533\ ms$) and ($T_1 = 119.54\ ms, T_2 = 8.5606\ ms$), relative to two population of spins with the NMr constraint $T_1 > T_2$.
The second relaxation map, named `3Pks` test, has 100×100 points. In this case the relaxation map, represented in Figure 1(b), has three peaks, relative to three population spins, with peaks in the following positions: ($T_1 = 1582.2\ ms, T_2 = 32.289\ ms$), ($T_1 = 5.9692\ ms, T_2 = 2.6124\ ms$) and ($T_1 = 1139.5\ ms, T_2 = 258.08\ ms$).
In both cases the number of the IR points is $M_1 = 128$, while for CPMG it is $M_2 = 2048$.
Normal Gaussian random noise $\mathbf{e}$ of level $\delta \equiv \|\mathbf{e}\|$ is added as follows: $\mathbf{s} = \mathbf{K}\mathbf{f}^* + \mathbf{e}$. The tests are carried out by running 10 noise realizations with $\delta = 10^{-2}$ and the numerical results reported in the table 1 and 2 are averaged over these noise realizations.
The algorithms accuracy is measured by means of the relative error $Erel^2$ and the Root Mean Squared Deviation $RMSD$, defined as follows:

$$Erel^2 = \|\mathbf{f} - \mathbf{f}^*\|^2 / \|\mathbf{f}^*\|^2, \quad RMSD = \frac{\|\hat{\mathbf{s}} - \mathbf{s}\|}{\sqrt{M}}, \quad \hat{\mathbf{s}} = \mathbf{K}\mathbf{f} \tag{31}$$

where $\mathbf{f}$ represents the map computed by the algorithms and $\mathbf{f}^*$ is the true map. The first analysis evaluates the effects of the multi-penalty and multi-parameter approach (L1LL2) compared to the L1 and multi-parameter L2 penalties. The adapted L1 penalty algorithm (A-L1) is obtained applying the algorithm 1 to solve (7) with $\lambda_i = 0$, while multi-parameter L2 is obtained by solving problem (3) with algorithm UPEN2D. In table 1, the error parameters and computation times are reported for each algorithm. While UPEN2D reaches always the most accurate solutions, the A-L1 algorithm has the greatest relative error values. Conversely, A-L1 is the fastest method while UPEN2D requires the longest computation times. We observe that L1LL2 achieves the best trade-off between accuracy and computation time. We can quantify such trade-off in terms of Percentage Accuracy Loss (PAL), defined as

$$PAL_m = \frac{Err_m - Err_{min}}{Err_{min}} \times 100 \tag{32}$$

where Err_m represents the relative error of method m (L1LL2 or A-L1) and Err_{min} is the minimum relative error, always obtained by UPEN2D. Analogously, we measure the Percentage Efficiency Gain (PEG) by subtracting the computation time of L1LL2 or A-L1 ($Time_m$) to that UPEN2D ($Time_{max}$):

$$PEG_m = \frac{Time_{max} - Time_m}{Time_{max}} \times 100 \tag{33}$$

The values reported in table 2 show that for the 2pks test the accuracy lost by L1LL2 is about 22% smaller than

Test	Algorithm	$Erel^2$ (-)	$RMSD$ (a.u.)	Time (s)
2Pks	L1LL2	$1.22\ 10^{-1}$	$1.953\ 10^{-4}$	10.80
	A-L1	$1.41\ 10^{-1}$	$1.953\ 10^{-4}$	10.13
	UPEN2D	$8.79\ 10^{-2}$	$1.953\ 10^{-4}$	68.6
3Pks	L1LL2	$1.09\ 10^{-1}$	$1.381\ 10^{-4}$	29.00
	A-L1	$1.31\ 10^{-1}$	$1.381\ 10^{-4}$	19.84
	UPEN2D	$8.51\ 10^{-2}$	$1.381\ 10^{-4}$	85.62

Table 1 Accuracy and computation times of the synthetic tests. Reference value $RMSD^* = \delta/\sqrt{M} = 1.9531\ 10^{-5}$.

Test	Algorithm	PAL (%)	PEG (%)
2Pks	L1LL2	38.8	84.3
	A-L1	60.5	85.2
3Pks	L1LL2	28.1	66.1
	A-L1	53.9	78.0

Table 2 Percentage Accuracy Loss (PAL (32)) and Percentage Efficiency Gain (PEG (33)) obtained by each method on the two different test problems.

A-L1 while the computation efficiency gained is similar. Concerning the 3Pks test we observe that accuracy lost by L1LL2 is about 25% smaller than A-L1 while the performance gained by A-L1 is 11% greater than that of L1LL2. Hence L1LL2 reaches the best balance between accuracy and computation time. This feature is well represented in figures 2 where the time evolution of $Erel^2$ is plotted for each algorithm. We observe that the introduction of the L_1 regularization causes a considerable decrease in the total computation time at the expenses of a slight increase in the relative error.

The contribution of the multi-parameter $L2$ term to the algorithm accuracy is further highlighted in figures 3 and 4 where the maps computed by the three algorithms on the 2Pks and 3Pks tests are shown. We observe that figures (b) and (d) are more precise in reproducing the true contour levels (figure (a)), compared to the A-L1 regularization algorithm in figure (c).

Concerning the residual values, we observe that the RMSD parameters reported in table 1 have indeed very tiny differences, in the range $[10^{-8}, 10^{-7}]$, revealing equal data consistency for all methods. Moreover the good results are confirmed by the RMSD correspondent to the true solution $\mathbf{f}^*$, given by $RMSD^* = \delta/\sqrt{M} = 1.9531\ 10^{-5}$.

4.2 Real data

In this section we report the reconstructions obtained with L1LL2 on real data acquisitions. Two measured samples are studied: a White Portland Cement (WPC) and a Maastricht stone, a limestone characterized by high porosity [9], (see [11], for a detailed description of acquisition parameters and instrument characteristics). The first test, named $T_1 - T_2$ test, is relative to an ^{1}H IR-CPMG measurement performed on a WPC sample

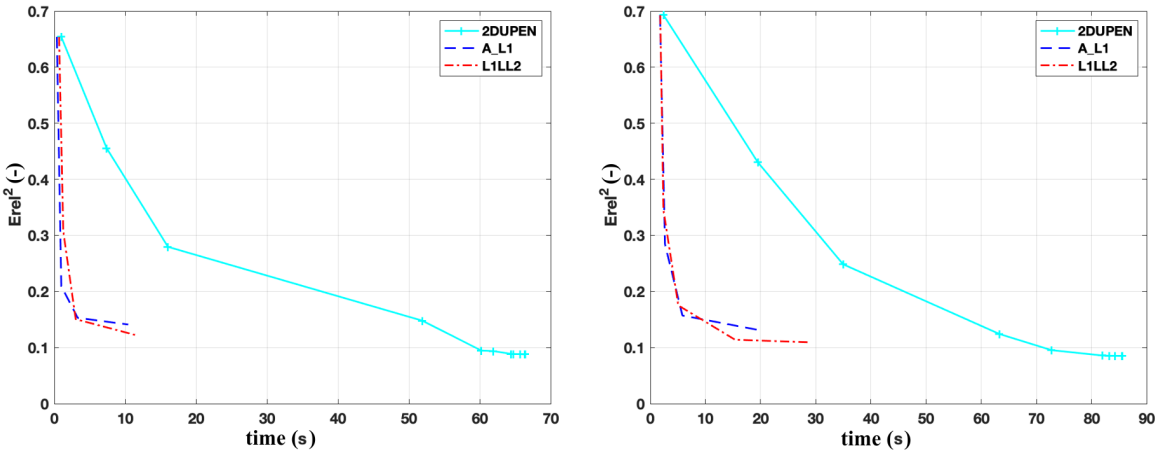

(a) Two peaks test (b) Three peaks test

Fig. 2 Relative Error vs. computation time: UPEN2D cyan line, A-L1, blue dashed line, L1LL2 red dash-dotted line.

Test	Algorithm	RMSD (a.u.)	$Erel_{UPEN2D}$ (-)	Time (s)
$T_1 - T_2$	L1LL2	$3.33\ 10^{-3}$	$9.36\ 10^{-2}$	4.2
	A-L1	$3.03\ 10^{-3}$	$3.91\ 10^{-1}$	6.5
	UPEN2D	$3.36\ 10^{-3}$	–	54.6
$T_2 - T_2$	L1LL2	$1.248\ 10^{-1}$	$1.99\ 10^{-1}$	4.32
	A-L1	$1.235\ 10^{-1}$	$5.00\ 10^{-1}$	7.85
	UPEN2D	$1.251\ 10^{-1}$	–	10.6

Table 3 RMSD, $Erel_{UPEN2D}$ and computation times obtained with 2D NMR real data.

hardened a few tens of minutes. The kernels are defined in (30), the data set have 48×1000 elements and the computed relaxation time map has 80×80 points. The second test, named $T_2 - T_2$ test is related to a ^{1}H CPMG-CPMG measurement performed on a Maastricht stone full saturated with water. In this case, both kernels k_1 and k_2 refer to transversal relaxation times T_{21}, T_{22} with the following expression:

$$k_1(t_1, T_{21}) = \exp(-t_1/T_{21}), \quad k_2(t_2, T_{22}) = \exp(-t_2/T_{22}).$$

and the T_1, T_2 in model (1) are substituted by T_{21}, T_{22}. The reconstructed relaxation time map has 64×64 points while the acquired data set has 128×2800 elements. Since in previous computations UPEN2D yielded the most accurate solutions on data set coming from different sequences and samples (see [10], [13], [14] and [11]), we use it as a reference method and we evaluat the following relative error $Erel_{UPEN2D}$:

$$Erel_{UPEN2D} = \frac{\|f - f_{UPEN2D}\|}{\|f_{UPEN2D}\|} \tag{34}$$

From the results reported in table 3 we observe that despite the similarity of the RMSD values within the same test problem, there is a remarkable difference in the relative distance from the reference solution computed by UPEN2D (column $Erel_{UPEN2D}$). Indeed $Erel_{UPEN2D}$ of A-L1 is always greater than that obtained by L1LL2. Moreover, the computation times show the improved efficiency of L1LL2, as expected.
In case of the $T_1 - T_2$ test, analysing the computed 2D contour map, figure 5, we can see two peaks with T_2 values at about 0.8 ms and 20 ms. As it well known, WPC pore structures depend on the sample preparation, and the hydration processes causes their continuously evolution over time, therefore these two peaks seem to be compatible with the population of spins into interhydrate spaces and capillary pores, respectively [25]. A small

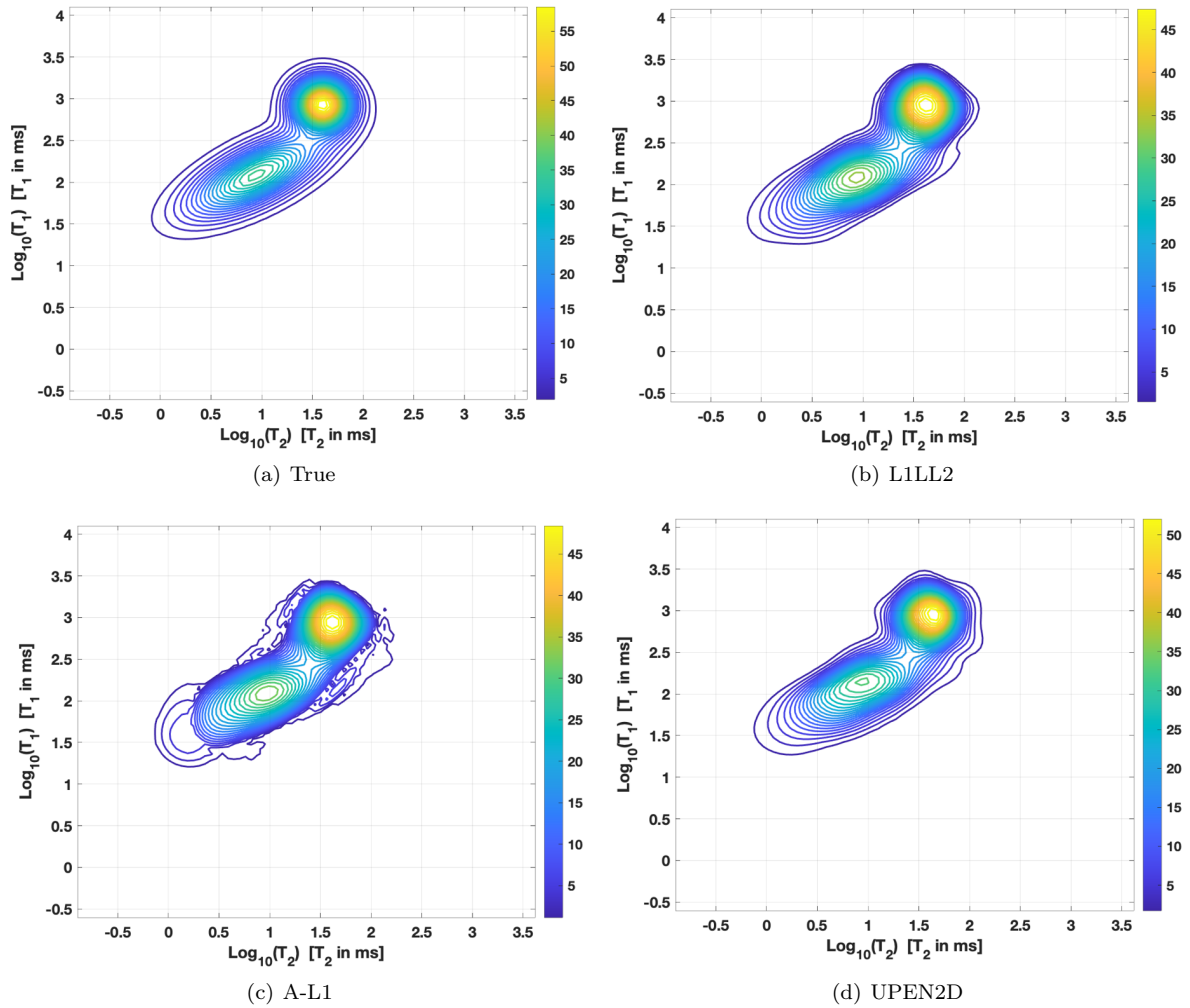

(a) True (b) L1LL2

(c) A-L1 (d) UPEN2D

Fig. 3 Contour plots of the 2pks test. (a) True distribution map, (b) L1LL2 reconstruction, (c) A-L1 reconstruction, (c) UPEN2D reconstruction.

artifact is visible in the contour map (figure 5) as well as in the T1 projection (figure 6). As a general comment, we can see the optimal correspondence of L1LL2 with UPEN2D in the 1D maps projections reported in figure 6 where both peaks are well defined in position, height and amplitude. The contour maps of the computed 2D relaxation time distributions, reported in figure 5, also confirm the good accuracy of L1LL2 compared to UPEN2D. We observe in figure 5(c) the poor A-L1 reconstruction, probably due to the low S/N ratio of the acquired data.

Concerning the $T_2 - T_2$ test, we again observe in table 3 the preservation of consistency of the results between L1LL2 and UPEN2D algorithms. The relaxation time contour maps, reported in figure 7, report a precise reproduction of spin population, confirmed also by the projection on horizontal axes in figure 8(b). Two-dimensional $T_2 - T_2$ exchange experiments are useful to assess exchange between different relaxation centers and to understand the pore connectivity. Off-diagonal peaks in figure 7 indicate exchange of water between pores of different size. While the peaks asymmetry can be caused by three-site exchange in the case of different exchange rates [26]. Concerning two smaller populations it is evident in figure 8(a) that relaxation maps are not coincident, however in this case L1LL2 provides a better separation of the spin populations with smaller relaxation times. Finally, we observe that L1LL2 is computationally more efficient than UPEN2D and A-L1

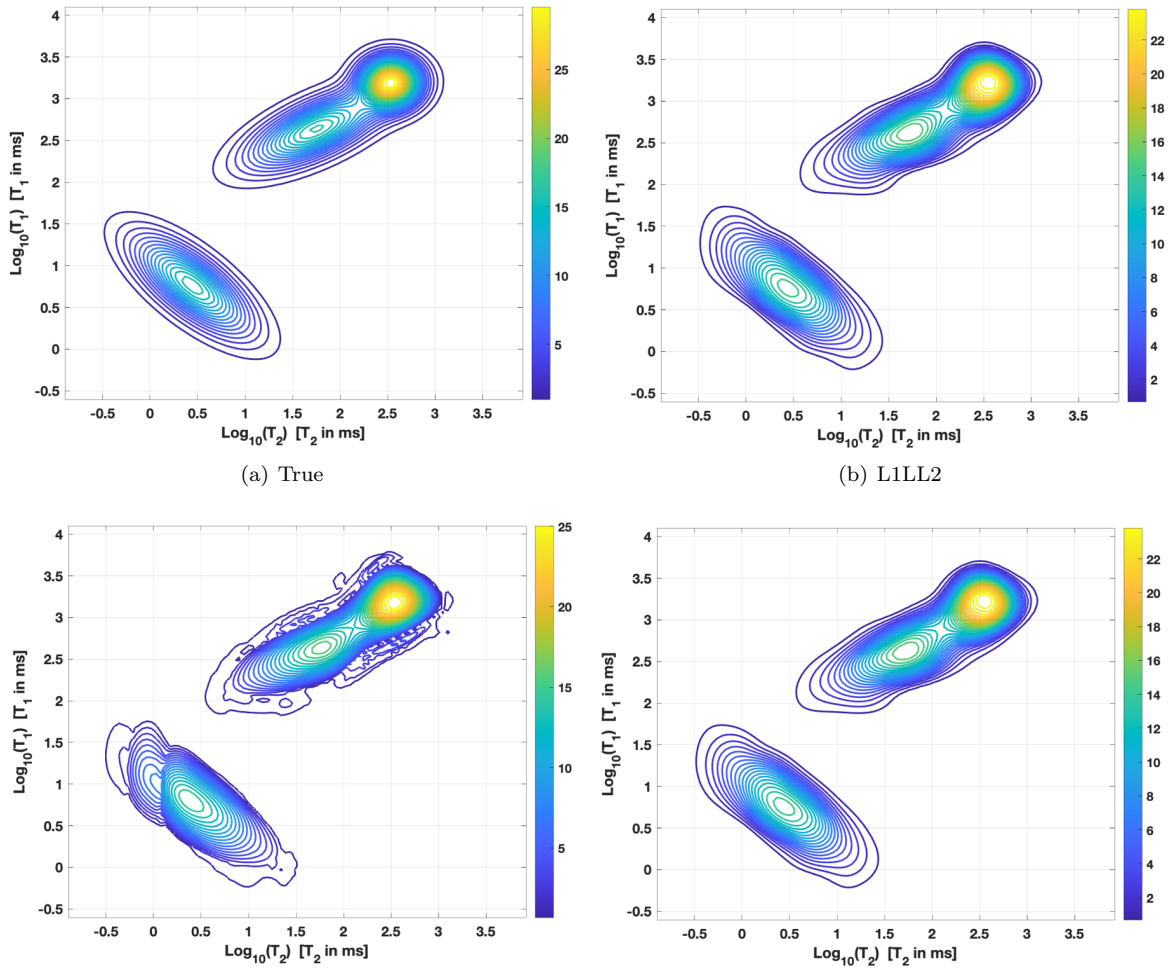

(a) True (b) L1LL2

(c) A-L1 (d) UPEN2D

Fig. 4 Contour plots of the 3pks test. (a) True distribution map, (b) L1LL2 reconstruction, (c) A-L1 reconstruction, (c) UPEN2D reconstruction.

map (figure 7(c)) suffers from evident distortions, probably due to the low S/N ratio of the acquired data. The 1D projections in figures 6, 8 are shown only for L1LL2 and UPEN2D because of the poor reconstructions computed by A-L1.

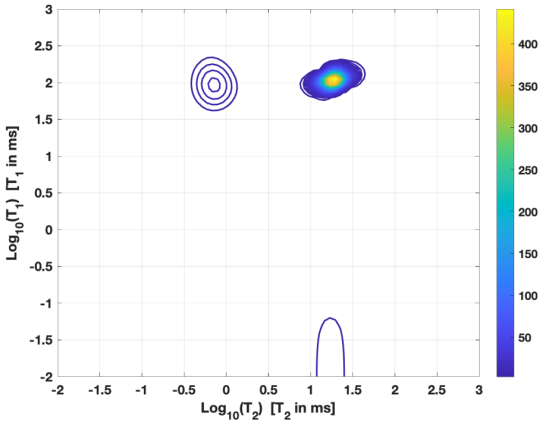

(a) UPEN2D

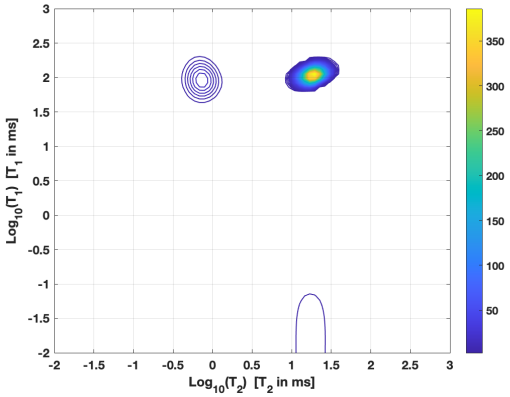

(b) L1LL2

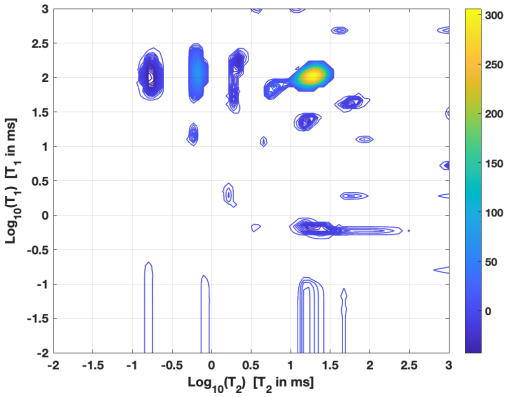

(c) A-L1

Fig. 5 Test $T_1 - T_2$, contour maps of relaxation times. (a) computed in 54.6 s. (b) computed in 3.53 s (c) computed in 6.6 s.

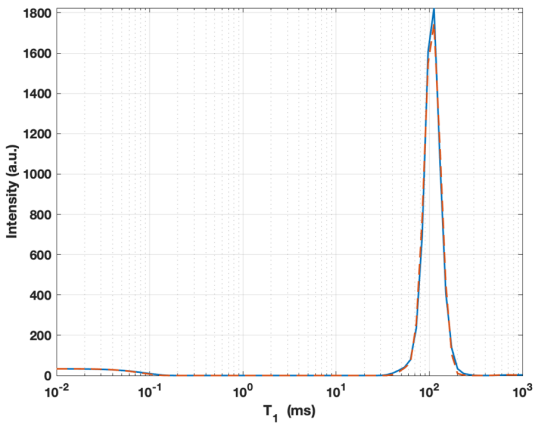

(a) T_1

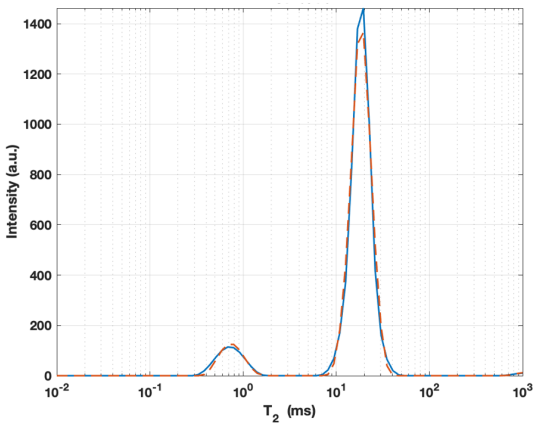

(b) T_2

Fig. 6 $T_1 - T_2$ test, projection of the time relaxation maps onto the vertical axis T_1 and onto the horizontal axis T_2. L1LL2 red dashed line, UPEN2D blue line.

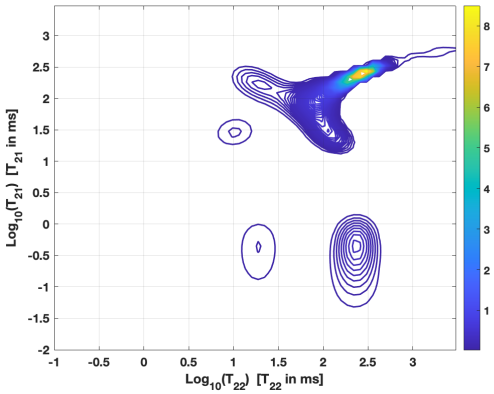

(a) UPEN2D

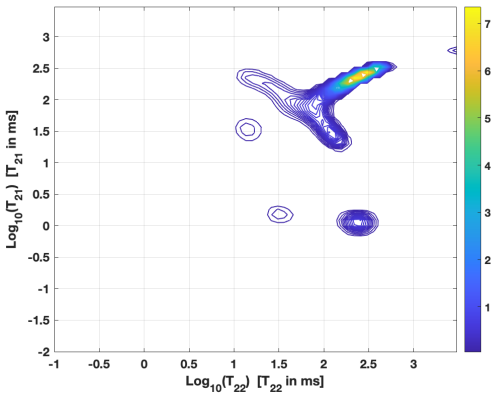

(b) L1LL2

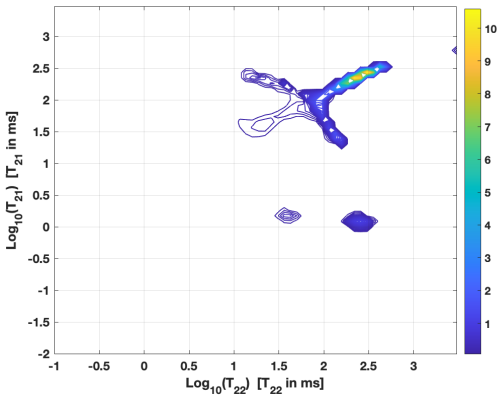

(c) A-L1

Fig. 7 Test $T_2 - T_2$, contour maps of relaxation times. (a) computed in 10.3 s, (b) computed in 3.6 s (c) computed in 7.8 s

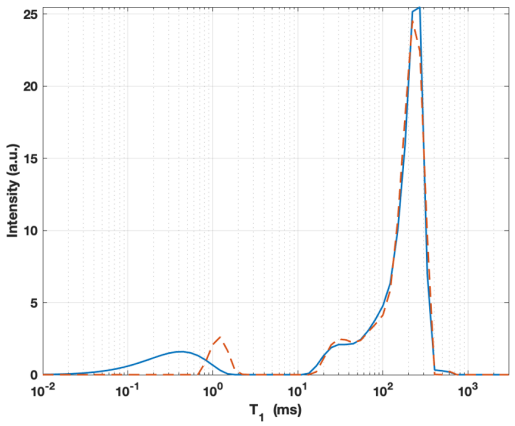

(a) T_{21}

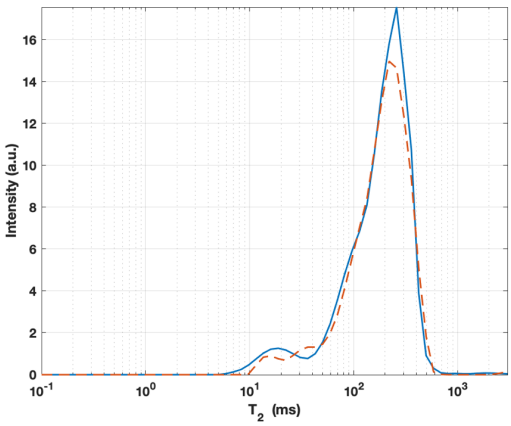

(b) T_{22}

Fig. 8 T2-T2 test, projection of the time relaxation maps onto the vertical axis T_{21} and onto the horizontal axis T_{22}. L1LL2 red dashed line, UPEN2D blue line.

5 Conclusion

This paper presents the L1LL2 method for the inversion of 2DNMR relaxation data. The algorithm automatically computes a 2D distribution map of NMR parameters and spatially adapted regularization parameters by iteratively solving a sequence of multi-penalty problems. The FISTA method is used for the solution of the minimization problems, and all the regularization parameters are updated according to the uniform penalty principle. The L1LL2 method has been compared to A-L1 and UPEN2D algorithms. The numerical results show that, compared to UPEN2D, the main advantage of L1LL2 is the increased computational speed without a significant loss in the inversion accuracy; compared to A-L1, L1LL2 provides more accurate distributions at a comparable computational cost. Future work will consider the extension of this method to different penalty functions to employ the generalized uniform Penalty principle to a broader variety of inverse problems.

Acknowledgements

This work was partially supported by Gruppo Nazionale per il Calcolo Scientifico - Istituto Nazionale di Alta Matematica (GNCS-INdAM).

References

1. C. Johnson, Borehole Nuclear Magnetic Resonance (NMR) 10.5066/F73J3BW0 .
2. K.J.Dunn and D.J. Bergman and G.A. Latorraca, Nuclear Magnetic Resonance: Petrophysical and Logging Applications. Elsevier 2002 ISBN:0080537790,9780080537795.
3. A. Beck, First-Order Methods in Optimization. MOS-SIAM Series on Optimization 978-1-61197-498-0.
4. J. Mitchell, L.F. Gladden, T.C. Chandrasekera, and E.J. Fordham, Low-field permanent magnets for industrial process and quality control. *Progress in Nuclear Magnetic Resonance Spectroscopy*, 76:1 – 60, 2014.
5. Y. Zhang, L. Xiao, X. Li, G. Liao, T1-D-T2 correlation of porous media with compressed sensing at low-field nmr, Magnetic Resonance Imaging 56 (2019) 174 – 180 doi:10.1016/j.mri.2018.09.028.
6. L. Venkataramanan, Y.-Q. Song, M. D. Hurlimann, Solving Fredholm integrals of the first kind with tensor product structure in 2 and 2.5 dimensions, IEEE Transactions on Signal Processing 50 (5) (2002) 1017–1026 doi:10.1109/78.995059.
7. J. P. Butler, J. A. Reeds, S. V. Dawson, Estimating solutions of first kind integral equations with nonnegative constraints and optimal smoothing, SIAM Journal on Numerical Analysis 18 (3) (1981) 381–397.
8. E. Chouzenoux, S. Moussaoui, J. Idier, F. Mariette, Primal-dual interior point optimization for a regularized reconstruction of NMR relaxation time distributions, in: 2013 IEEE International Conference on Acoustics, Speech and Signal Processing, 2013, pp. 8747–8750.
9. L. Brizi, M. Camaiti, V. Bortolotti, P. Fantazzini, B. Blümich and S. Haber-Pohlmeier, One and two-dimensional NMR to evaluate the performance of consolidants in porous media with a wide range of pore sizes: Applications to cultural heritage, *Microporous and Mesoporous Materials*, (269), (2018),186–190, doi:10.1016/j.micromeso.2017.08.014.
10. V. Bortolotti, R. J. S. Brown, P. Fantazzini, G. Landi, F. Zama, Uniform penalty inversion of two-dimensional NMR relaxation data, Inverse Problems 33 (1) (2016) 015003 doi:10.1088/1361-6420/33/1/015003.
11. V. Bortolotti, L. Brizi, P. Fantazzini, G. Landi, F. Zama, Upen2DTool: A Uniform PENalty Matlab tool for inversion of 2D NMR relaxation data, SoftwareX 10 (2019) 100302 doi:https://doi.org/10.1016/j.softx.2019.100302.
12. D. Bertsekas, Projected Newton methods for optimization problem with simple constraints, SIAM J. Control Optim. 20 (2) (1982) 221–245.
13. V. Bortolotti, L. Brizi, P. Fantazzini, G. Landi, F. Zama, Filtering techniques for efficient inversion of two-dimensional Nuclearhttps://www.overleaf.com/project/5feb4e23a42b000518e150db Magnetic Resonance data, Journal of Physics: Conference Series 904 (2017) 012005 doi:10.1088/1742-6596/904/1/012005.
14. V. Bortolotti, R. J. S. Brown, P. Fantazzini, G. Landi, F. Zama, I2DUPEN: Improved 2DUPEN algorithm for inversion of two-dimensional NMR data, Microporous and Mesoporous Materials 269 (2018) 195 – 198, proceedings of the 13th International Bologna Conference on Magnetic Resonance in Porous Media (MRPM13). doi:https://doi.org/10.1016/j.micromeso.2017.04.038.
15. X. Zhou, G. Su, L. Wang, S. Nie, X. Ge, The inversion of 2D NMR relaxometry data using L1 regularization, Journal of Magnetic Resonance 275 (2017) 46 – 54. doi:https://doi.org/10.1016/j.jmr.2016.12.00.
16. A. Beck, M. Teboulle, A Fast Iterative Shrinkage-Thresholding Algorithm for linear inverse problems, SIAM Journal on Imaging Sciences 2 (1) (2009) 183–202. doi:10.1137/080716542.
17. D. Lazzaro, E. L. Piccolomini, F. Zama, A fast splitting method for efficient Split Bregman iterations, Applied Mathematics and Computation 357 (C) (2019) 139–146.
18. D. Lazzaro, E. L. Piccolomini, F. Zama, A nonconvex penalization algorithm with automatic choice of the regularization parameter in sparse imaging, Inverse Problems 35 (8) (2019) 084002 doi:10.1088/1361-6420/ab1c6b.
19. Y. Wu, C. D'Agostino, D. J. Holland, L. F. Gladden, In situ study of reaction kinetics using compressed sensing NMR, Chem. Commun. 50 (2014) 14137–14140 doi:10.1039/C4CC06051B.

20. P. D. Teal, C. Eccles, Adaptive truncation of matrix decompositions and efficient estimation of NMR relaxation distributions, Inverse Problems 31 (4) (2015) 045010 doi:10.1088/0266-5611/31/4/045010.
21. H. Zou, T. Hastie, Regularization and variable selection via the elastic net, J. R. Statist. Soc. B 67 (2) (2005) 301–320.
22. P. Berman, O. Levi, Y. Parmet, M. Saunders, Z. Wiesman, Laplace inversion of low-resolution NMR relaxometry data using sparse representation methods, Concepts in Magnetic Resonance Part A 42 (3) (2013) 72–88 doi:10.1002/cmr.a.21263.
23. S. Campisi-Pinto, O. Levi, D. Benson, M. Cohen, M. T. Resende, M. Saunders, C. Linder, Z. Wiesman, Analysis of the regularization parameters of primal–dual interior method for convex objectives applied to 1H low field Nuclear Magnetic Resonance data processing, Applied Magnetic Resonance 49 (10) (2018) 1129–1150 doi:10.1007/s00723-018-1048-4.
24. K. Miller, Least squares methods for ill-posed problems with a prescribed bound, SIAM J. Math. Anal. 1 (1970) 52–74.
25. K. Scrivener, R. Snellings and B. Lothenbach, (Eds.) A Practical Guide to Microstructural Analysis of Cementitious Materials (1st ed.), CRC Press,(2016) doi:10.1201/b19074.
26. M. Van Landeghem, A. Haber, J,B. D'espinose De Lacaillerie, B. Blümich, Analysis of multisite 2D relaxation exchange NMR *Concepts Magn. Reson., 36A: (2010), 153-169* doi:10.1002/cmr.a.20157.